AER/AGS Open File Report 2024-02

Alberta Energy Regulator

Moment Tensor Analysis for the Local Magnitude 3.7 Seismic Event on June 25, 2022, Near Hinton, Central Alberta

AGS
ALBERTA GEOLOGICAL SURVEY

AER/AGS Open File Report 2024-02

Moment Tensor Analysis for the Local Magnitude 3.7 Seismic Event on June 25, 2022, Near Hinton, Central Alberta

H. Bui[1,2], V.H. Stern[1], J.A. Yusifbayov[1], M. Reyes Canales[1] and N.L. Roman[1]

[1] Alberta Energy Regulator
Alberta Geological Survey
[2] University of Alberta

April 2024

©His Majesty the King in Right of Alberta, 2024
ISBN 978-1-4601-5716-9

The Alberta Energy Regulator / Alberta Geological Survey (AER/AGS), its employees and contractors make no warranty, guarantee, or representation, express or implied, or assume any legal liability regarding the correctness, accuracy, completeness, or reliability of this publication. Any references to proprietary software and/or any use of proprietary data formats do not constitute endorsement by the AER/AGS of any manufacturer's product.

If you use information from this publication in other publications or presentations, please acknowledge the AER/AGS. We recommend the following reference format:

Bui, H., Stern, V.N., Yusifbayov, J.A., Reyes Canales, M. and Roman, N.L. (2024): Moment tensor analysis for the local magnitude 3.7 seismic event on June 25, 2022, near Hinton, central Alberta; Alberta Energy Regulator / Alberta Geological Survey, AER/AGS Open File Report 2024-02, 27 p.

Publications in this series have undergone only limited review and are released essentially as submitted by the authors.

Published April 2024 by:
Alberta Energy Regulator
Alberta Geological Survey
Suite 205
4999 – 98 Avenue NW
Edmonton, AB T6B 2X3
Canada

Tel: 780.638.4491
Email: AGS-Info@aer.ca
Website: ags.aer.ca

Contents

Tables

Figures

Acknowledgements

The authors would like to thank Chris Filewich (Alberta Geological Survey), Todd Shipman, and Alexandra Robertson (Alberta Energy Regulator) for their constructive discussions when performing the analysis. We would also like to thank Sheila Stewart, Matt Grobe, and Andrew Beaton (Alberta Geological Survey) for their comments and suggestions, which greatly improved the report.

Abstract

Source mechanisms help understand the faulting behaviour and the evolving stress field in the subsurface. This study investigates the source mechanism of an event with a local magnitude (M_L) of 3.7 that occurred near a blasting site, 19 km east of Hinton, central Alberta, on June 25, 2022. It seeks to demonstrate how moment tensor analysis can be used to discriminate between mining blast–related events and tectonic events (earthquakes) in Alberta. The amplitude-based method was used to invert the seismic moment tensor of the event. The amplitudes of compressional P-waves and shear S-waves recorded at multiple seismic stations of regional networks were used in the inversion. The synthetic amplitudes of the ground displacements were computed using ray tracing and a one-dimensional velocity model. Then the solution was found through a least-squares inversion scheme. The inverted moment tensors of the M_L = 3.7, June 25, 2022, event were compared with the inverted moment tensors of six suspected blasts and an earthquake (M_L = 1.68) near Hinton. The analysis revealed that the M_L = 3.7, June 25, 2022, event was a blast. It was neither a natural earthquake unrelated to the blasting nor an event induced by a blast as initially suspected.

1 Introduction

On June 25, 2022, at 23:31 UTC, a seismic event with a local magnitude (M_L) of 3.7 occurred near a blasting site, 19 km east of Hinton, central Alberta. Due to the large magnitude of this event, an investigation was initiated to determine if the event was a mining blast, a natural earthquake, or an event triggered by blasting.

The aim of this study was to classify the event by analyzing its source mechanism using moment tensor inversion. Moment tensor analysis provides an advanced understanding of faulting behaviour and how the stress field evolves in the subsurface (Baig and Urbancic, 2010; Eaton et al., 2014; Eyre and van der Baan, 2015). Firstly, the essential source parameters of seismic events, including faulting types, orientations, and magnitudes, are retrieved (Eyre and van der Baan, 2015). Then it is possible to determine if the event's source mechanism relates to volumetric changes (i.e., explosions or implosions) or shearing motion on a fault. It is also possible to calculate the event's moment magnitude (M_W), a quantitative measure of a seismic event's strength, and estimate the event's M_L from the M_W using scaling relations (Ross et al., 2016; Yenier, 2017).

For the moment tensor analysis, seismic data from multiple stations in several regional seismic networks accessible by the Alberta Geological Survey (AGS) were used. To categorize the event type, the results of the analysis of the June 25, 2022, event were compared with the analyses of six suspected blasts (in 2022) and an earthquake (EQ) event (M_L = 1.68) near Hinton (in 2016).

2 Theory

2.1 Seismic Moment Tensor

In mathematics, a tensor is an algebraic object analogous to but more general than a vector, and is represented by an array of components that are functions of space coordinates. In seismology, moment tensors are used to mathematically describe the various seismic sources. A seismic moment tensor consists of nine force couples of different orientations (Stein and Wysession, 2003; Forouhideh and Eaton, 2009). Since the moment tensor depends on the fault orientation and the source strength, it characterizes all information about the source (Stein and Wysession, 2003; Forouhideh and Eaton, 2009). The nine force couples of the moment tensor are denoted in a square 3 by 3 matrix as follows (Aki and Richards, 2002):

$$M = M_0 \begin{bmatrix} M_{11} & M_{12} & M_{13} \\ M_{21} & M_{22} & M_{23} \\ M_{31} & M_{32} & M_{33} \end{bmatrix}, \quad (1)$$

where M_0 denotes the seismic moment and M_{ij} represents the force couples, where i, j = [1, 2, 3]. The seismic moment tensor is symmetrical, with only six independent components, including M_{11}, M_{22}, M_{33}, M_{12}, M_{13}, and M_{23}. The three diagonal elements represent force couples that describe volumetric changes. The off-diagonal elements form balanced double-couples and describe shearing motion.

2.2 Beachball Representation

Seismic moment tensors are illustrated graphically using beachball plots. Beachball plots are projections of the compressional P-wave radiation pattern on a horizontal plane of the lower half of an imaginary spherical shell (also known as a focal sphere) surrounding the seismic source (Eyre and van der Baan, 2015). The beachball plot has two regions: compression (pressure), often denoted by the black colour, and dilation (tension), often represented by the white colour. Figure 1a–c displays beachball plots of the focal mechanisms for three common fault types, including strike-slip fault (shear), normal fault (extension), and reverse fault (compression).

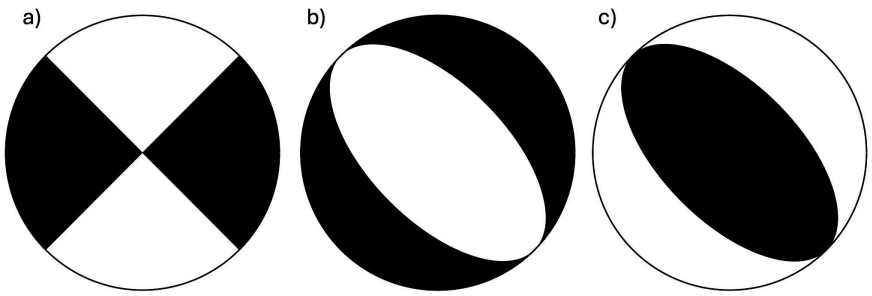

Figure 1. Examples of beachball plots of focal mechanisms for common fault types: (a) strike-slip, (b) normal, (c) reverse. The black colour represents the compression region, and the white colour represents the dilation region.

2.3 Seismic Source Mechanisms

The seismic source mechanisms can be classified into two main groups: double-couple (DC) sources and non–double-couple sources. The DC sources describe shear faulting and do not involve any volumetric change (Stein and Wysession, 2003; Forouhideh and Eaton, 2009). Most earthquakes are caused by shear faulting and are generally assumed to have DC source mechanisms (Stein and Wysession, 2003; Forouhideh and Eaton, 2009). A DC moment tensor has two characteristics: (1) one eigenvalue is zero and (2) the trace of the tensor is also zero (Stein and Wysession, 2003; Forouhideh and Eaton, 2009).

Unlike the DC sources, which do not involve volumetric change, the non-DC sources are related to volumetric changes (Stein and Wysession, 2003; Forouhideh and Eaton, 2009). The non-DC sources can be categorized into two components: the isotropic (ISO) component and the compensated linear vector dipole (CLVD) component (Forouhideh and Eaton, 2009). A purely volumetric source is an ISO source (Forouhideh and Eaton, 2009). This source is described using a seismic moment tensor that contains equal-valued nonzero diagonal elements and zeroes for the off-diagonal elements (Forouhideh and Eaton, 2009). In other words, the ISO moment tensor comprises three vector dipoles of three equal and orthogonal force couples, representing the equivalent body force system for an explosion or implosion (Forouhideh and Eaton, 2009). The CLVD source, which corresponds to uniaxial compression or tension, has one dipole that is -2 times the magnitude of other dipoles (Forouhideh and Eaton, 2009). Typical DC, ISO, and CLVD moment tensors and their associated focal mechanisms (represented by beachball plots) can be found in Stein and Wysession (2003).

3 Methodology

3.1 Overview of Moment Tensor Inversion Methods

Three main moment tensor inversion methods, commonly described in the literature, are the first-arrival polarity method, the amplitude-based method, and the full-waveform method (Eyre and van der Baan, 2015). This subsection elaborates on the advantages and disadvantages of each method.

1) The first-arrival polarity approach uses the polarities of the first-arrival P-wave and the receiver locations to determine the orientation of the source mechanism, as described in Eyre and van der Baan (2015). For regional seismic networks, the seismic stations are near the surface; thus, the recorded upward first motions correspond to compressional first arrivals, and the downward first motions correspond to dilatational first arrivals. The first-arrival polarity method is the quickest and simplest to implement but also the crudest method; it has the least constraints on the orientation of the mechanism due to the binary nature of the polarities (up or down). Therefore, many possible inversion results can equally fit the data. This method usually assumes the source mechanism to be DC, which causes difficulties in resolving complex source mechanisms, that is, combined shear and

tensile faulting. Identifying the P-wave onsets for surface monitoring data is often challenging because the P-waves often have weak amplitudes and are embedded in various noise sources (i.e., noise from strong wind and traffic).

2) The amplitude-based approach better constrains the moment tensor inversion than the first-arrival polarity method (Hardebeck and Shearer, 2003; Eyre and van der Baan, 2015). Amplitude data is not binary and has a range of values (Hardebeck and Shearer, 2003). Furthermore, using both P- and S-wave amplitudes in the inversion increases the number of observations and produces more reliable inversion results (Hardebeck and Shearer, 2003). The S/P amplitude ratios can provide additional information on the source type. An S/P ratio of less than five indicates that tensile failure is the most likely source, and a ratio greater than five shows that shear failure is the most likely source (Eaton et al., 2014). The amplitudes are influenced by several factors, such as geometric spreading, attenuation, and station site effects, which should be considered for more reliable inversion results (Eyre and van der Baan, 2015). Additionally, picking the P- and S-wave arrivals might be difficult when the signals are embedded in high-amplitude noise.
3) The full-waveform approach uses entire waveform data from all components recorded at the seismic stations to invert the moment tensor, as described in Eyre and van der Baan (2015). This method is more precise than the first-arrival polarity and amplitude-based methods. The propagation effects can be removed by modelling the propagation of seismic waves between source and receiver locations as accurately as possible, producing Green's functions. Green's functions are the signals that would arrive at the receivers if the source-time function was a delta function. However, the full-waveform method requires a good knowledge of three-dimensional (3D) velocity models and calculating Green's functions can also be computationally expensive. The inversion only works well for low-frequency data and becomes unstable at higher frequencies. Additionally, the station site effects must be considered when using this method.

3.2 Moment Tensor Inversion Using an Amplitude-Based Method

Eyre and van der Baan (2017) demonstrated that using seismic amplitudes recorded by surface monitoring arrays could constrain reliable moment tensor inversion results. The recorded seismic amplitudes at stations are the convolution results between the event's source mechanism and the propagation effects through the medium (Eyre and van der Baan, 2017); thus, they contain valuable information on the source characteristics. Considering the advantages and disadvantages of the methods described in Section 3.1, the amplitude-based method was selected to perform the moment tensor analysis for this study. The P- and S-wave amplitudes picked from the recorded data, not the whole waveforms, were used to run the inversion. The theory of the amplitude-based method is similar to the 3D full-waveform inversion; however, the former is simpler and it can avoid issues with high-frequency data. The following subsections describe the steps of the inversion workflow using the amplitude-based method, from data preprocessing, to velocity model building, to Green's function calculation, to inverting the moment tensors.

3.2.1 Seismic Data Preprocessing

1) Unit conversion: raw time-series seismic data often have units of counts, which is the number read off the physical instrument (i.e., the voltage read from a seismometer). The counts are converted into m/s by dividing all three data components by a scale factor. The scale factor varies depending on the instrument installed at the station and can be obtained from the instrument's properties. For an instrument with a scale of 3.275×10^9 counts, 1 unit equals 1 m/s (Seismological Facility for the Advancement of Geoscience, 2018). The converted data in the m/s unit are then used for the next step.
2) Signal detrend: removing trends from a time-series dataset is called detrending. Usually, raw seismic data recorded at the stations are not centred on the x-axis. The mean value of the data is subtracted

from the original time-series data to centre the signal around the x-axis and is then used for the next step.

3) Noise filtering: this step reduces unwanted noise in the data and improves the signal-to-noise ratio (SNR) by filtering. Since the amplitudes are the inputs for the inversion, care must be taken when designing the filter. The preferred option is to minimize the involvement of filters as much as possible and preserve the signals (Maxwell, 2014). A high-pass filter, which keeps signals with frequencies higher than a certain cutoff value, can be used.
4) Displacement data calculation: normally, the seismic data recorded at the stations are ground velocities since seismometers are often installed near the surface. Sometimes, ground accelerations are recorded if accelerometers are used. Since the moment tensor inversion algorithm uses the ground displacement amplitudes, it is necessary to integrate the data (velocity or acceleration) to obtain ground displacements. The Riemann integral method is used to integrate the data once (if the data are velocities) or twice (if the data are accelerations). The Riemann integral is defined in terms of Riemann sums of functions with respect to tagged partitions of an interval. A Riemann sum, S, of a time series, $f(x)$, is defined as

$$S = \sum_{i=1}^{N} f(x_i)\Delta t, \tag{2}$$

where $f(x_i)$ is element i^{th} of the time series $f(x)$ that has N time samples, and Δt is the sample rate (Anton, 1999).

5) Picking P- and S-wave arrivals and defining time windows: after obtaining the ground displacement data, the P- and S-wave arrivals are picked and the time windows that contain the maximum absolute amplitudes of the P- and S-waves are defined. Different types of seismic phases are present on the seismogram, including body waves and surface waves (Bormann et al., 2012). The body waves, including compressional P-waves (longitudinal waves) and shear S-waves (transverse waves), propagate through the interior of the Earth. These waves are, therefore, affected strongly by refraction, reflection, and mode conversion at the main boundaries (e.g., Moho discontinuity), which separate geological layers with strong contrast in density and velocity (Bormann et al., 2012). The surface waves travel near the Earth's surface and have lower frequencies and larger amplitudes than body waves (Bormann et al., 2012). It is necessary to understand these arrivals properly to identify the phases correctly. The P-wave onsets are often hard to pick due to their weak amplitudes, but the S-waves are easier to identify as they often have stronger energy and larger amplitudes. With the P- and S-wave arrival picks, the lengths of the windows, which contain the first peak (maximum value) or trough (minimum value) of the P- and S-waves, can be defined. The starts of the windows are the P- and S-wave time arrivals. The ends of the windows depend on the waveforms; the windows could be 100–300 time samples or longer to include the maximum absolute amplitude. However, the surface waves must not be included in the window.

3.2.2 One-Dimensional Velocity Model Building

The building of the velocity model is one of the critical aspects of the moment tensor inversion workflow. To construct the one-dimensional (1D) velocity model, the mean value of vertical velocities within a layer is obtained from compressional and shear sonic logs with the use of a blocking technique. Due to seismic anisotropy, the seismic velocity is faster in the horizontal direction than in the vertical direction (Van Dok et al., 2011). Thus, a velocity calibration is often applied to obtain the appropriate velocity models. After obtaining the 1D velocity model with multiple layers, linear interpolation, a common approach to estimating values at positions between known data points, is used to create a 1D velocity model with the desired interval (i.e., values at every 10 m).

The 1D layered velocity model can be used to calculate the travel times and distances of P- and S-waves along the ray paths by implementing a 1D ray-bending algorithm (Červený, 2001). Then, the average P- and S-wave velocities along the ray path are computed and used in the next step.

3.2.3 Green's Function Calculation

Green's functions are calculated using the equations for particle motion generated by the P- and S-wave radiations from a point source in a homogeneous elastic medium (Aki and Richards, 2002). The P- and S-wave amplitudes recorded on a given receiver at position *x* and time *t* are given as

$$a_i^P(x,t) = \frac{1}{4\pi r\rho\alpha^3}\{\gamma_i\gamma_j\gamma_k M_{jk}\}, \tag{3}$$

$$a_i^S(x,t) = \frac{1}{4\pi r\rho\beta^3}\{(\delta_{ij} - \gamma_i\gamma_j)\gamma_k M_{jk}\}, \tag{4}$$

where i, j, k = x, y, z; r is the source to receiver distance; ρ is the density; α and β are the P- and S-wave velocities, respectively, obtained from the previous step; $\gamma_i, \gamma_j, \gamma_k$ are the directions cosine from the source to the receiver; M is the moment tensor; and δ_{ij} is the Kronecker delta (Aki and Richards, 2002; Eyre and van der Baan, 2017).

3.2.4 Moment Tensor Inversion

To invert the elements of the moment tensor, first, the amplitudes in Equations (3) and (4) are rewritten in a matrix form as follows:

$$\begin{bmatrix} d_1 \\ d_2 \\ \vdots \\ d_n \end{bmatrix} = \begin{bmatrix} G_{11} & G_{12} & G_{13} & G_{14} & G_{15} & G_{16} \\ \vdots & \vdots & \vdots & \vdots & \vdots & \vdots \\ \vdots & \vdots & \vdots & \vdots & \vdots & \vdots \\ G_{n1} & G_{n2} & G_{n3} & G_{n4} & G_{n5} & G_{n6} \end{bmatrix} \begin{bmatrix} m_1 \\ m_2 \\ \vdots \\ m_6 \end{bmatrix}, \tag{5}$$

where d_i are the observed ground displacement amplitudes at different arrival times at receiver i (i = 1: n, n is the number of receivers); G is an *n* by 6 matrix containing the calculated Green's functions (synthetic amplitudes of ground displacements), and m_i are the six elements, M_{11}, M_{22}, M_{33}, M_{12}, M_{13}, and M_{23}, of the moment tensor (Forouhideh and Eaton, 2009). The least-squares method is then used to find an approximate solution to the system of *n* linear equations (Equation 5). The solution (Menke, 1989; Eyre and van der Baan, 2017) can be given as follows:

$$m = (G^T G)^{-1} G^T d, \tag{6}$$

where T indicates a matrix transpose, provided $(G^T G)^{-1}$ exists (i.e., provided G has full column rank). This formula finds an approximate solution when no exact solution exists, and it gives an exact solution when one does exist.

3.3 Moment Tensor Decomposition and Visualization

3.3.1 Decomposition

To facilitate the interpretation of the inverted moment tensor, it is decomposed into elementary components. A common approach is to decompose it into ISO, CLVD, and DC components as follows (Knopoff and Randall, 1970; Jost and Herrmann, 1989; Forouhideh and Eaton, 2009):

$$M = M^{ISO} + M^{CVLD} + M^{DC}, \tag{7}$$

where *M* is the full moment tensor obtained from the least-squares method (Equation 6) with nine elements in the form of a 3 by 3 square matrix. The M^{ISO}, M^{CVLD}, and M^{DC} are the percentage of ISO, CVLD, and DC components, respectively, and are given as follows:

$$M^{ISO} = \frac{1}{3} tr(M) \begin{bmatrix} 1 & 0 & 0 \\ 0 & 1 & 0 \\ 0 & 0 & 1 \end{bmatrix}, \quad (8)$$

$$M^{CLVD} = |\varepsilon| M^{*}_{|max|} \begin{bmatrix} -1 & 0 & 0 \\ 0 & -1 & 0 \\ 0 & 0 & 2 \end{bmatrix}, \quad (9)$$

$$M^{DC} = (1 - 2|\varepsilon|) M^{*}_{|max|} \begin{bmatrix} -1 & 0 & 0 \\ 0 & 0 & 0 \\ 0 & 0 & 1 \end{bmatrix}, \quad (10)$$

where $tr(M)$ denotes the trace of the square matrix *M*, which is the sum of its eigenvalues; M^{*} is the deviatoric component of the moment tensor and is the sum of the CLVD and DC components; and ε is a dimensionless quantity defined as

$$\varepsilon = -\frac{M^{*}_{|min|}}{M^{*}_{|max|}}, \quad (11)$$

where $M^{*}_{|max|}$ and $M^{*}_{|min|}$ are the maximum and minimum values of the deviatoric component.

For a pure CLVD source, $\varepsilon = \pm 0.5$ and for a pure DC source $\varepsilon = 0$. Also, ε is positive for tensile sources and negative for compressional sources (Forouhideh and Eaton, 2009). The sum of the ISO and CLVD components is called the non-DC component. Based on the proportion of these elementary components, inverted moment tensors can be interpreted and some basic types of sources can be identified (Vavryčuk, 2015). Explosion and implosion sources are isotropic, and are characterized by 100% ISO and 0% CLVD and DC (Vavryčuk, 2015). Shear faulting is characterized by 100% DC and 0% ISO and CLVD (Vavryčuk, 2015). Pure tensile or compressive faulting is free of shearing and thus characterized by 0% DC (Vavryčuk, 2015). The ISO and CLVD components have the same sign: they are positive for tensile faulting but negative for compressive faulting (Vavryčuk, 2011). A shear-tensile (dislocation) source is defined as a source that combines both shear and tensile faulting (Vavryčuk, 2011) and is characterized by nonzero ISO, CLVD, and DC components. The positive values of ISO and CLVD correspond to tensile mechanisms when the fault is opening during rupturing (Vavryčuk, 2015). The negative values of ISO and CLVD correspond to compressive mechanisms when the fault is closing during rupturing (Vavryčuk, 2015).

3.3.2 Hudson's Source–Type Plot

The moment tensor decomposition can be represented using different plots, such as the diamond source–type plot, Hudson's source–type plot, and Riedesel-Jordan's source–type plot (Vavryčuk, 2015). In this study, the Hudson's source–type plot (Figure 2) is used to visually represent the decomposition results. The Hudson's source–type plot displays the relative proportions of the ISO, CLVD, and DC elemental sources. The vertical axis of Hudson's source–type plot is the ISO component, from -100% implosion to 100% explosion. The horizontal axis is the deviatoric decomposition, from +100% to -100% CLVD, with 100% DC in the centre (0% ISO and CLVD; Hudson et al., 1989). The outer border is the 0% DC line (Hudson et al., 1989).

The DC (shear) mechanisms are plotted in the centre of Hudson's source–type plot. Explosive and implosive events are located at the top and bottom of Hudson's source–type plot, respectively, whereas opening and closing tensile crack mechanisms are on the top-left and bottom-right edges of the diagram, respectively (Hudson et al., 1989). The Hudson's source–type plot can be used to assess the uncertainties of the ISO, CLVD, and DC components. The moment tensor is usually plotted as a cluster of acceptable solutions on a Hudson's source–type plot, and the cluster's size reflects the uncertainties of the solutions (Eyre and van der Baan, 2017).

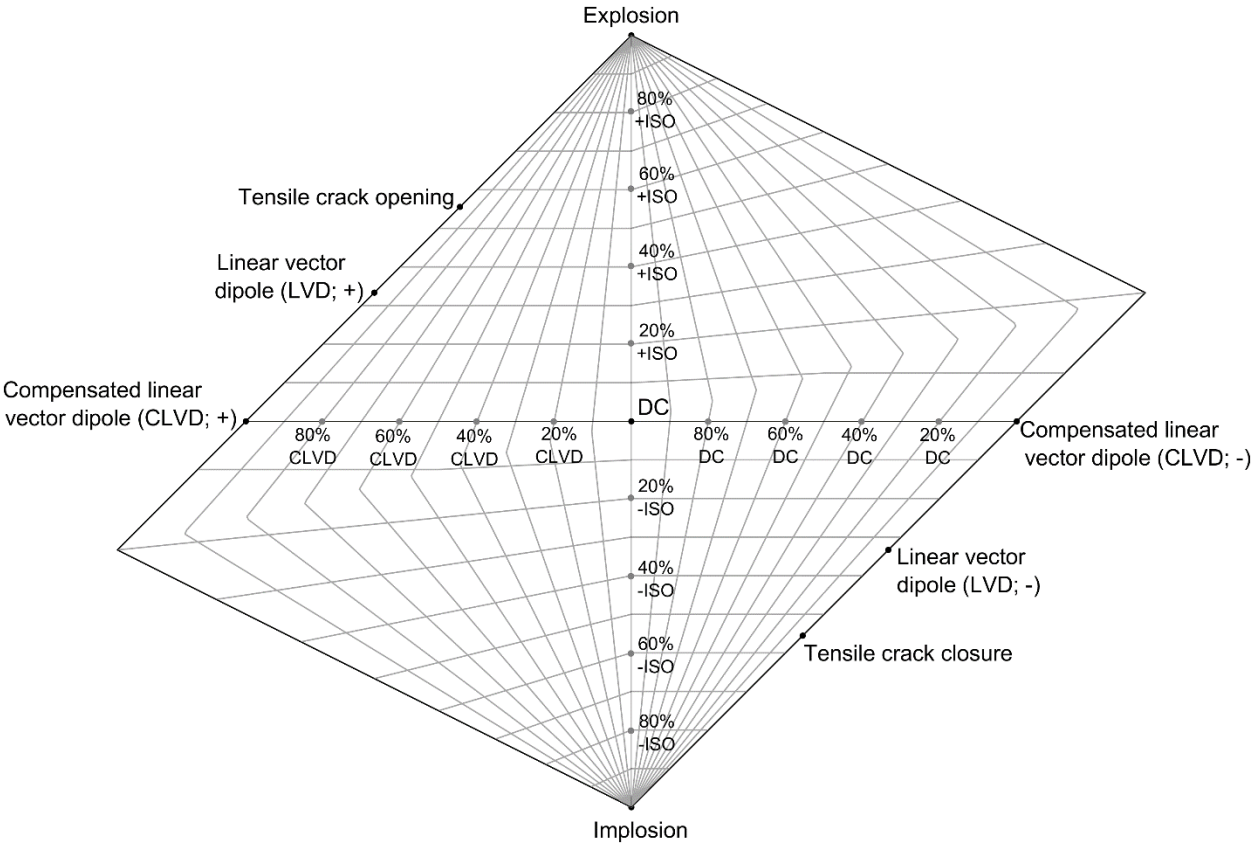

Figure 2. Hudson's source–type plot (modified after Hudson et al., 1989). Abbreviations: DC, double couple; ISO, isotropic.

3.4 Moment Magnitude Estimation

The moment magnitude, M_W, can be derived from M_0 using (Stein and Wysession, 2003)

$$M_w = \frac{2}{3} log_{10}(M_0) - 6.07, \quad (12)$$

where M_0 is the seismic moment obtained from the moment tensor inversion (Equation 1). The moment magnitude can also be estimated from the M_L and a magnitude scaling relation between M_W and M_L proposed by Ross et al. (2016) as follows:

$$M_w = 0.754 M_L + 0.88. \quad (13)$$

4 Implementation and Results

4.1 Data Overview

The station data were acquired from the EarthScope Consortium public database using Boulder Real Time Technologies, Inc.'s Antelope environmental data collection software. The compiled data are of ground velocity recorded as three-component miniSEED data, usually defined as HHE (east), HHN (north), and HHZ (vertical), by the seismometers at the seismic stations. The data were obtained in a table format for preprocessing, inverting moment tensors, and calculating the decomposition.

Since the amplitudes of the seismic waves were used to invert the moment tensors, data with good station coverage were needed to obtain reliable inversion results. The station data should also have a good SNR and visible P- and S-phases. Table 1 lists the seismic stations that recorded the data used in this moment tensor analysis. The source mechanisms of the M_L = 3.7, June 25, 2022, event, six suspected blasts, and an EQ event near Hinton in 2016 were all analyzed. The suspected blasts were classified as blasting events based on their location (i.e., proximity to the known quarries), timing (i.e., during typical blasting hours), and operational status of the nearby quarry. These seismic stations are part of four seismic networks, including the Regional Alberta Observatory for Earthquake Studies Network (RAVEN; Schultz and Stern, 2015), Scientific Induced Seismicity Monitoring Network (SCISMN; Schultz et al., 2020), TransAlta Monitoring Network (TD), and Montana Regional Seismic Network (MRSN; D'Alessandro and Stickney, 2012). Figure 3 shows the locations of the stations and events. Note that the azimuthal coverage of the seismic stations relative to the event precluded data acquisition southwest of the event.

4.2 Implementation

4.2.1 Seismic Data Preprocessing

This section describes how the three-component raw seismic data were preprocessed to prepare the inputs for moment tensor inversion. Figure 4a shows an example of 24-hour three-component raw seismic data recorded by the BDMTA station (RAVEN) on June 25, 2022. The data have two horizontal components, HHE and HHN, and a vertical component, HHZ.

As the data were supplied in units of counts (Figure 4a), the first step was converting the units into m/s (unit of velocity) by dividing all three data components by the scale factor for the instrument. This step is necessary because the input for the inversion is ground displacement derived from velocity data. The scale factor for each instrument was found in the dataless file provided with the downloaded data. The dataless file also contained further information on the instrument, such as location and sample rate. Table 4 in Appendix 1 shows the scale factors of the instruments used for the inversion.

Table 1. Seismic stations in central Alberta that recorded the data used in this moment tensor analysis. See Table 4 in Appendix 1 for station details. Abbreviations: EQ, earthquake; M_L, local magnitude.

Event	Number of Stations	Stations
June 25, 2022, M_L = 3.7	18	DEDWA, EGLEA, FAIRA, HSPGA, KW003, KW006, KW008, KW010, LDM, PECRA, TD008, BRLDA, SNUFA, TONYA, BDMTA, STPRA, TD002, WTMTA
Blast 1	9	BDMTA, BRLDA, KAKWA, KW002, KW008, SNUFA, TD002, TD008, TONYA
Blast 2	9	BRLDA, EGLEA, FAIRA, KAKWA, KW002, KW003, SNUFA, TD002, WTMTA
Blast 3	6	EGLEA, KAKWA, KW002, SNUFA, SWHSA, YELLA
Blast 4	10	BDMTA, BRLDA, EGLEA, KW002, KW003, SWHSA, TD002, TD008, TD009, YELLA
Blast 5	5	BRLDA, EGLEA, KW002, KW003, YELLA
Blast 6	8	KAKWA, KW002, KW003, KW008, SWHSA, TD002, TD008, YELLA
2016 EQ	4	TD09A, TD011, TD013, TD029

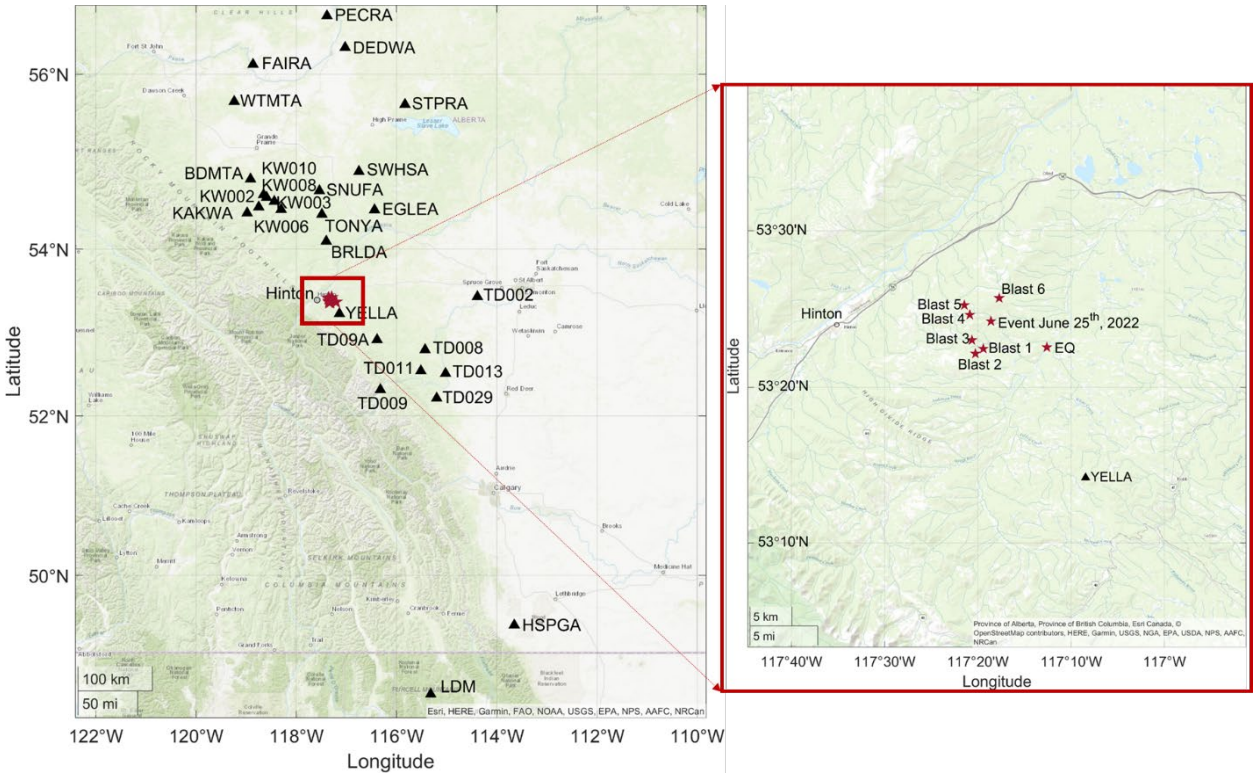

Figure 3. Locations of seismic stations, the local magnitude (M_L) 3.7, June 25, 2022, event, six suspected blasts, and the earthquake (EQ) event (M_L = 1.68) near Hinton, May 4, 2016, central Alberta (exact coordinates can be found in Appendix 1, Tables 4 and 5).

Next, the time-series data were detrended by subtracting the mean value to remove the signal offset and centre the data around the x-axis. Then the unwanted noise in the data was attenuated using high-pass filtering to improve the data quality. This step was helpful since the seismometers are installed at a very shallow depth, approximately 1 m, and high-amplitude noise from various sources, such as wind, and traffic and other human activities, are present in the data. However, caution was taken when designing the filter to avoid signal loss and preserve the signal's amplitudes for the inversion. A high-pass filter with a cutoff frequency of 1 hertz (Hz) was applied in this study. Figure 4b shows the preprocessed data, including the M_L = 3.7 event, after unit conversion, signal detrend, and noise filtering. A zoomed in section of the event (Figure 4c) shows the improved data quality, with clear P- and S-phases. After that, the resulting data were integrated using Equation 1 to obtain the ground displacement (unit of m). Finally, the P- and S-wave arrivals were picked and used to define the time windows that contain the maximum absolute amplitudes of these phases (Figure 4d).

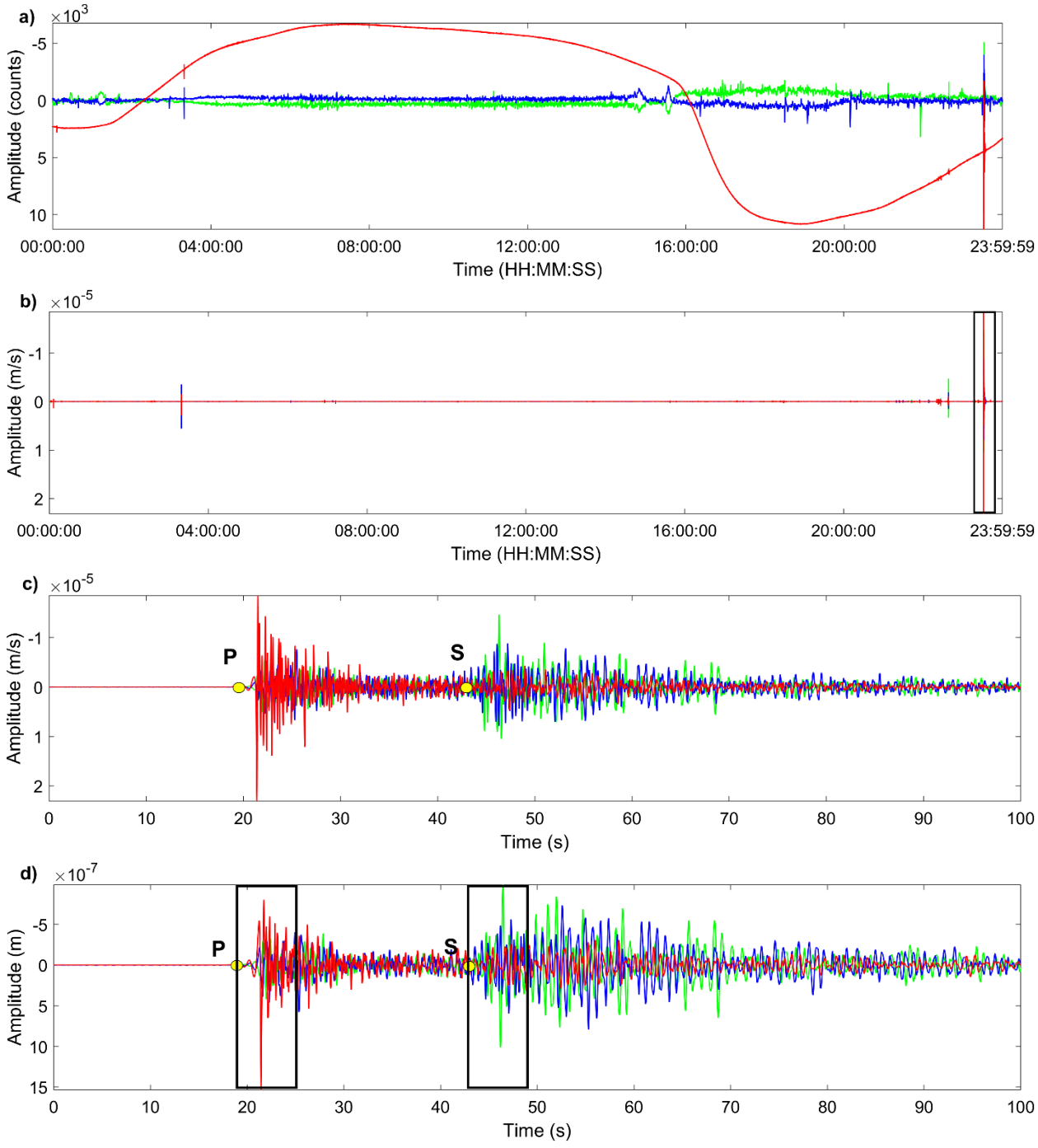

Figure 4. Examples of the preprocessing steps taken to prepare the data for the moment tensor inversion. (a) Twenty-four–hour three-component raw seismic data recorded by the BDMTA station on June 25, 2022. (b) Preprocessed seismic data (after unit conversion, signal detrend, and noise filtering). The black rectangle shows the local magnitude 3.7 event. (c) A zoomed in section of the preprocessed seismic data for the event. The P- and S-wave picks are now clear. (d) Ground displacement data with P- and S-wave windows highlighted by black rectangles. All of the seismic data have two horizontal components, HHE (east) in green and HHN (north) in blue, and a vertical component, HHZ in red. Yellow dot indicates the onset of the P- or S-waves. Abbreviations: HH, hour; MM, minute; SS, second.

Table 2. Details of the layers in the one-dimensional velocity model for the Hinton area, central Alberta. Abbreviations: V_P, P-wave velocity; V_S, S-wave velocity.

Layer	Depth (km)	V_P (km/s)	V_S (km/s)
1	0	2	0.85
2	0.05	3.4	1.96
3	1.276	5.15	2.97
4	2.976	6.1	3.53
5	15.776	6.5	3.71

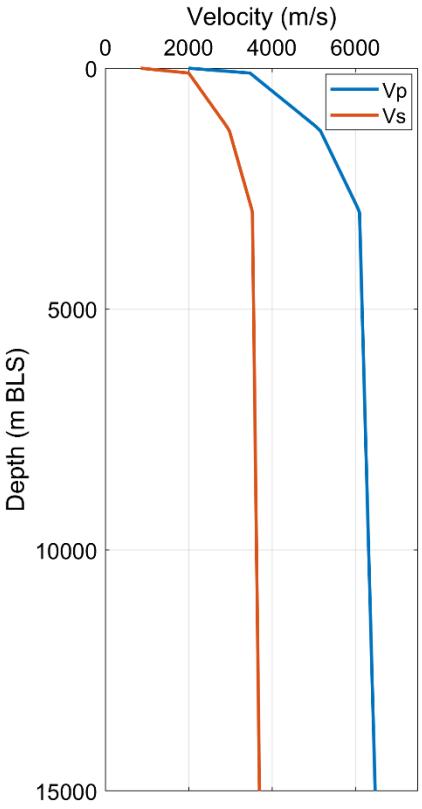

Figure 5. One-dimensional interpolated velocity model for the Hinton area, central Alberta. Abbreviations: BLS, below land surface; V_P, P-wave velocity; V_S, S-wave velocity.

4.2.2 Velocity Model Building

This section describes how the 1D layered velocity model was constructed. The AGS has built 1D velocity models for different areas in the province, such as Fox Creek, Rocky Mountain House, and Red Deer, using composite studies of well logs and crust models. The velocity model for this study has five layers (Table 2); linear interpolation was used to generate the velocity values at every 10 m. Figure 5 shows the interpolated 1D velocity model. This model was used to compute the travel time and distance of P- and S-waves along the seismic ray paths, using a 1D ray-bending algorithm.

4.2.3 Green's Function Calculation

The next step was to calculate Green's functions using Equations 3 and 4. Seismic wave amplitudes recorded at the stations can be approximated by the convolution between the source mechanisms

mathematically represented by moment tensors and the propagation effects described by Green's functions (Eyre and van der Baan, 2015). Computing Green's functions produces the synthetic displacement responses arriving at the stations when an impulse force (Kronecker delta) is applied at the source (Eyre and van der Baan, 2015). In other words, this step provided the synthetic amplitudes needed for the inversion in the next step. The P- and S-wave velocities used in Equations 3 and 4 are the average velocities along the ray computed using the travel times and distances calculated in the previous step. Since density does not change drastically with depth, a constant density value, ρ = 2850 kg/m^3, was used. The moment tensor was not required for Green's function calculation, so an arbitrary moment tensor, with a value of one for the three diagonal elements and a value of zero for the other elements, was used.

4.2.4 Moment Tensor Inversion

After obtaining the preprocessed seismic data and the synthetic displacements from Green's functions calculation, the inversion was run and the six independent elements of the moment tensors, including M_{11}, M_{22}, M_{33}, M_{12}, M_{13}, and M_{23}, were obtained through a least-squares solution (Equation 6). As the data were recorded at multiple stations, the consistency in the results between the stations is the key to evaluating the inversion's reliability.

4.2.5 Moment Tensor Decomposition

Using the six independent elements of the moment tensor obtained from the previous step, the full moment tensor was rearranged as follows:

$$M = M_0 \begin{bmatrix} M_{11} & M_{12} & M_{13} \\ M_{12} & M_{22} & M_{23} \\ M_{13} & M_{23} & M_{33} \end{bmatrix}. \quad (14)$$

The resulting moment tensor was then decomposed into three elementary components, ISO, CLVD, and DC, to facilitate the interpretation of the source type and evaluate the uncertainties of the inversion results. The percentage of ISO component, M^{ISO}, was computed using Equation 8. Then the deviatoric moment was computed using

$$M^* = M - M^{ISO}. \quad (15)$$

With the maximum and minimum M^* values, the quantity ε was computed using Equation 11. Then, with the maximum M^* values and ε values, the percentages of CLVD and DC components were computed using Equations 9 and 10, respectively.

4.3 Results

4.3.1 Moment Tensor Analysis for the M_L = 3.7, June 25, 2022, Event

Figure 6a and b shows the moment tensor inversion results for the June 25, 2022, event on a beachball plot and Hudson's source–type plot, respectively. The beachball plot (Figure 6a) shows a mixed mode source (not pure explosion/implosion or pure shearing) with a large compressive region (represented by the black colour). Seventy-two percent of the stations (13 out of 18 stations) used in the analysis yielded the moment tensor solutions plotted in the positive linear vector dipole corner of the Hudson's source–type plot (Figure 6b).

Table 6 in Appendix 1 shows the moment tensor decomposition results for the data from all 18 stations. The percentages of ISO, CLVD, and DC components are also plotted in Figure 7. A strong consistency is evident in the results from the 18 stations, with a large non-DC component and a small DC component, indicating reliable inversion results. The CLVD component (linear dilatation) has the highest average value, with 58.9% of the full moment tensor, followed by the ISO component with 29.4%, and the DC with 11.7%.

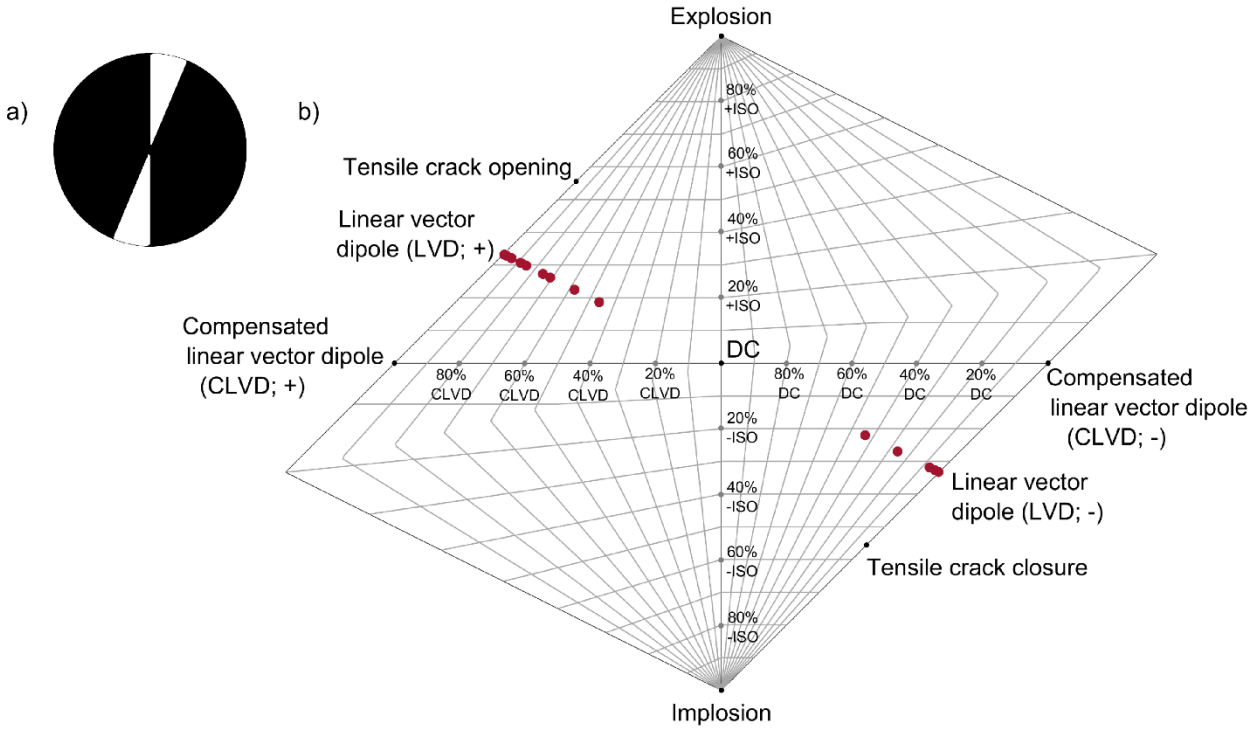

Figure 6. Moment tensor inversion results for the local magnitude 3.7, June 25, 2022, event: (a) beachball plot; (b) Hudson's source–type plot with solutions shown as red dots. Abbreviations: DC, double couple; ISO, isotropic.

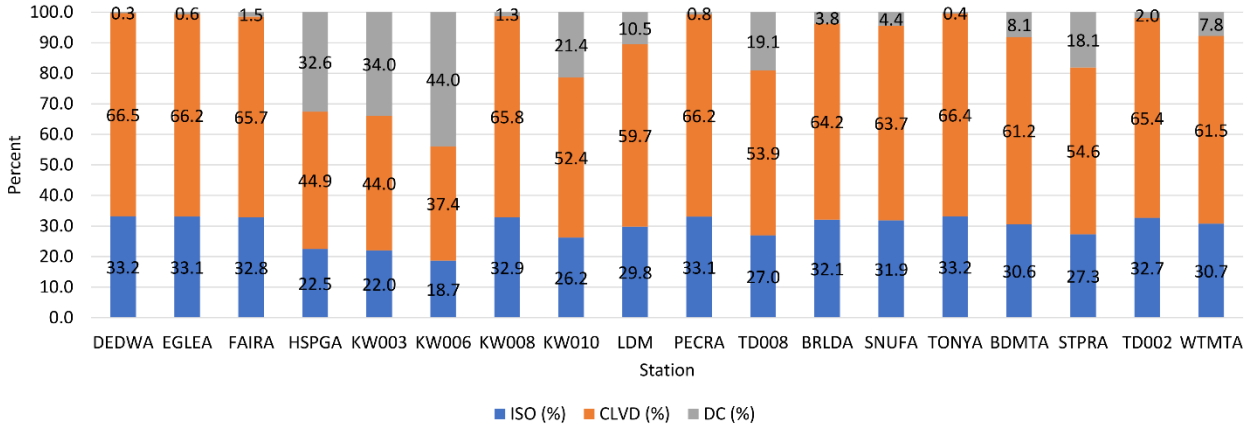

Figure 7. Moment tensor decomposition results for the local magnitude 3.7, June 25, 2022, event. See Figure 3 for locations of event and stations. Abbreviations: CLVD, compensated linear vector dipole; DC, double-couple; ISO, isotropic.

4.3.2 Moment Tensor Analysis for Six Suspected Blast Events

Figure 8a and b shows the moment tensor inversion results on the beachball plot and Hudson's source–type plot of a suspected blast. Data from six blasts were analyzed but only the results from blast 2 have been plotted as an example. The beachball plot (Figure 8a) shows a mixed mode source (not pure explosion/implosion or pure shearing) with a large compressive region (represented by the black colour). Seventy-eight percent of the stations (seven out of nine stations) used in the analysis generated the moment tensor solutions plotted in the positive linear vector dipole corner of Hudson's source–type plot (Figure 8b).

The decomposition results of the full moment tensors of six suspected blasts are shown in Figure 9a–f and Tables 7–12 in Appendix 1. Similar results are seen from the six blasts and at the different stations for each of the blasts, implying reliable inversion results. The average of absolute values for the six suspected blasts exhibit a significant non-DC component, from approximately 75% (blasts 3 and 6) to >90% (blast 2) of the full moment tensors. The DC component only accounts for a small proportion (<27%) of the full moment tensors. For example, the DC component for blast 2 is <10%, indicating that the shearing motion on the nodal plane was negligible. A small DC component is expected in the source mechanism of a blast. Kühn and Vavryčuk (2013) demonstrated that the presence of shear faulting triggered during blasting could not be excluded from the full moment tensor.

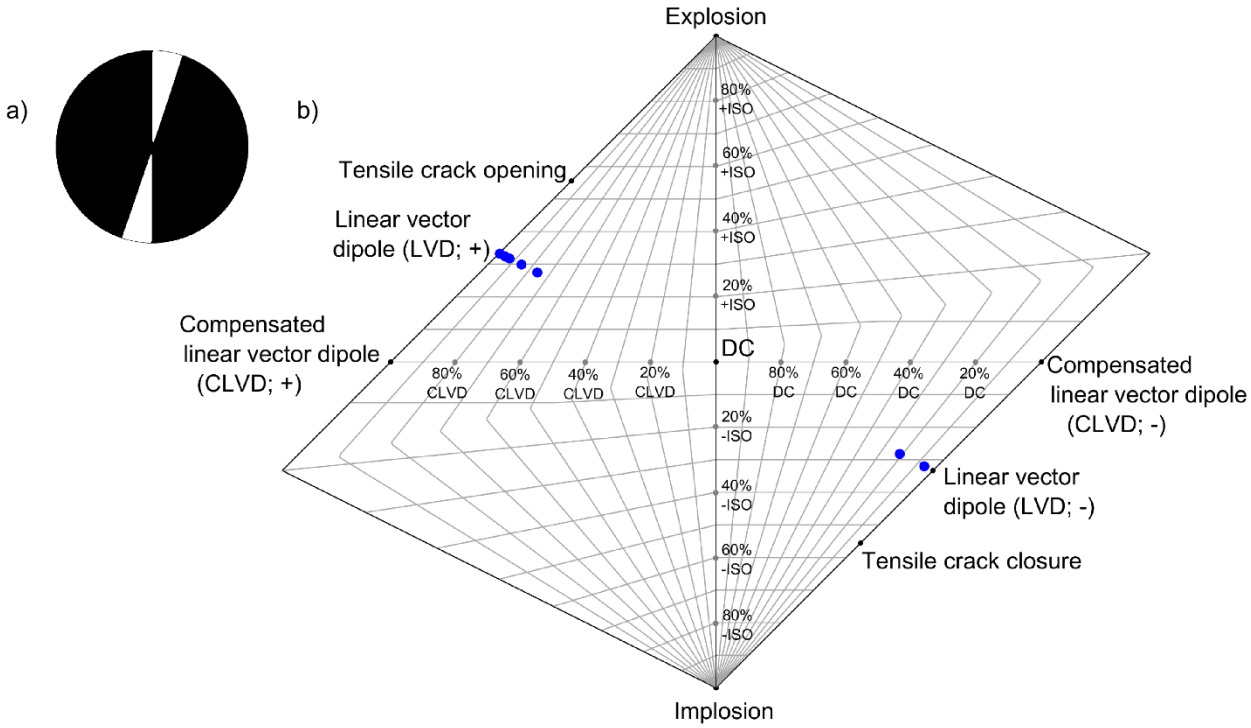

Figure 8. Moment tensor inversion results for blast 2, one of six suspected blasts analyzed. As similar signatures were observed for all six blasts, the results of blast 2 have been plotted as representative: (a) beachball plot; (b) Hudson's source–type plot with solutions shown as blue dots. Abbreviations: DC, double couple; ISO, isotropic.

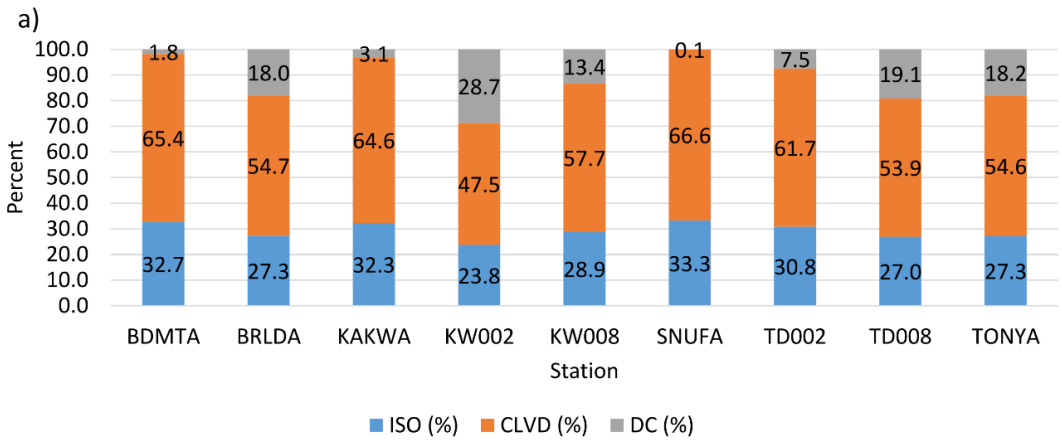

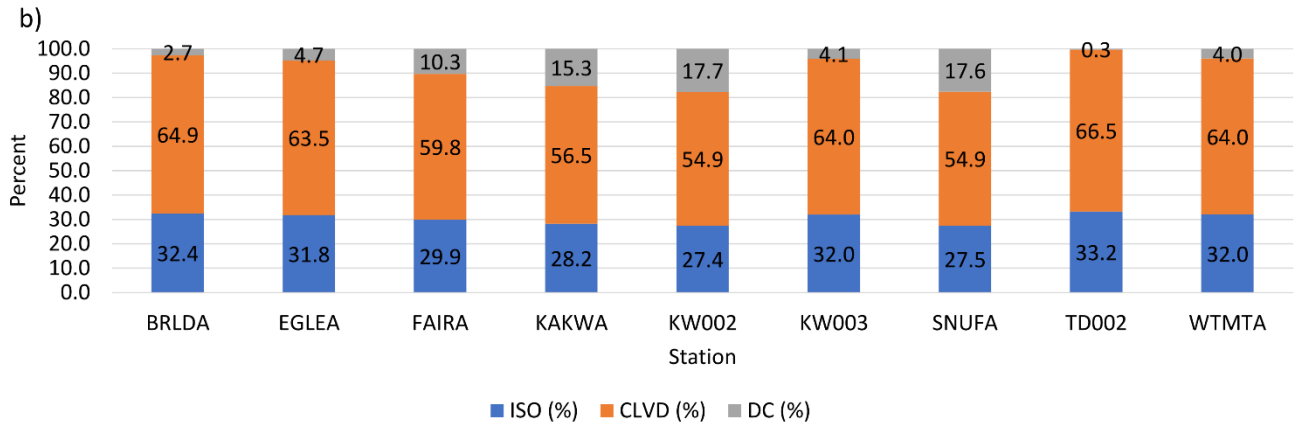

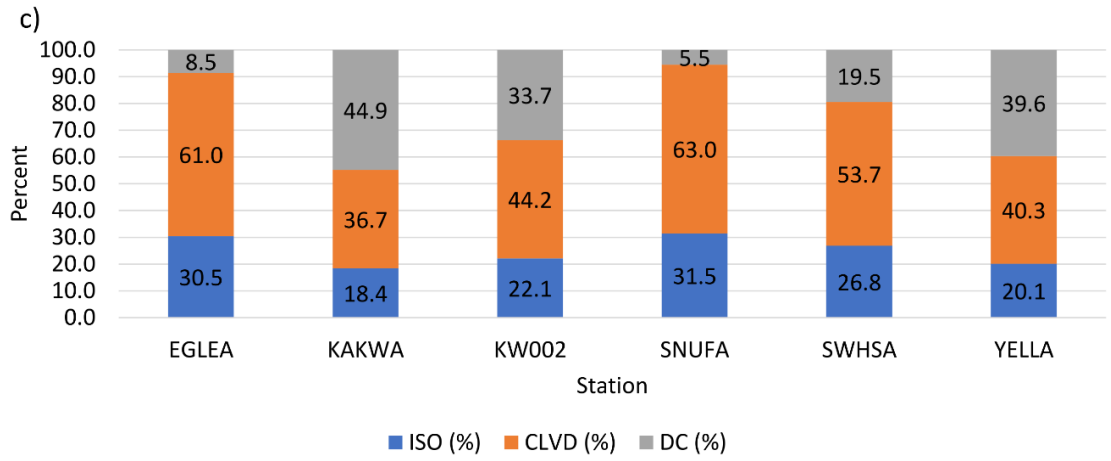

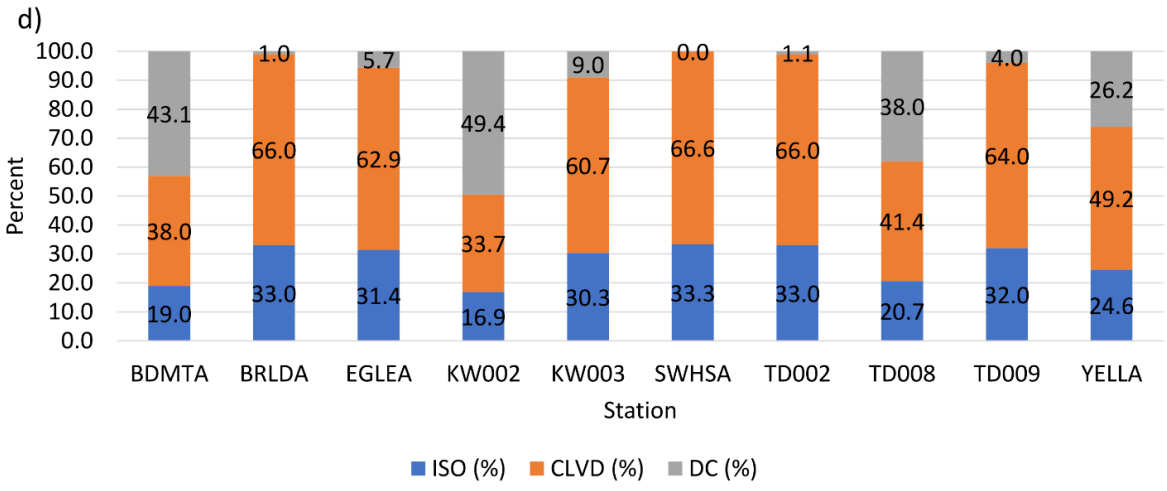

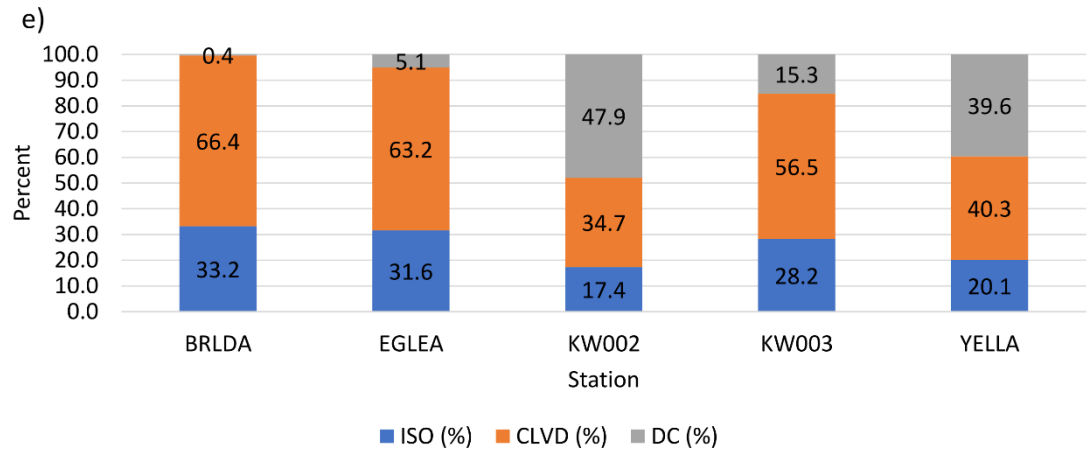

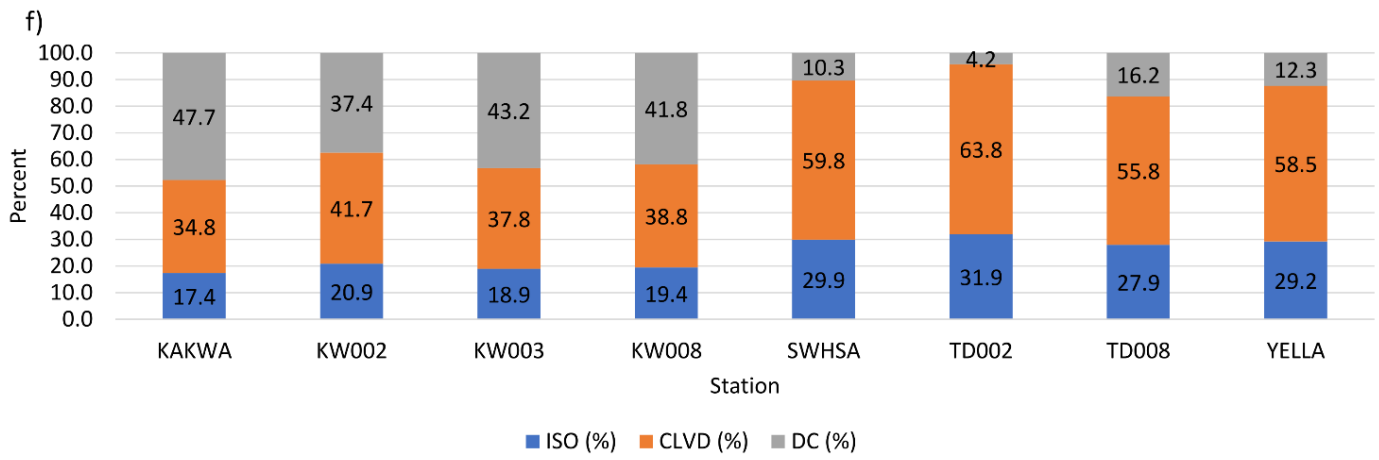

Figure 9. Moment tensor decomposition results for six suspected blasts: (a) blast 1, April 24, 2022; (b) blast 2, April 30, 2022; (c) blast 3, May 23, 2022; (d) blast 4, July 8, 2022; (e) blast 5, July 16, 2022; (f) blast 6, July 19, 2022. See Figure 3 for locations of events and stations. Abbreviations: CLVD, compensated linear vector dipole; DC, double-couple; ISO, isotropic.

4.3.3 Moment Tensor Analysis for an Earthquake (M_L = 1.68) Event near Hinton in 2016

Figure 10a and b shows the moment tensor inversion results for the EQ event near Hinton on May 4, 2016, on a beachball plot and Hudson's source–type plot. The beachball plot (Figure 10a) shows a strike-slip event. The inverted moment tensor solutions all plotted in the centre of the Hudson's source–type plot, indicating a DC source mechanism. The decomposition results of the full moment tensors of the EQ event are shown in Figure 11 and Table 13 in Appendix 1. There is a strong consistency in the data from the different stations. The EQ event exhibits a substantial DC component, ~80%, and a small non-DC component, ~20%, in the full moment tensor.

4.3.4 Comparison

To classify the ML = 3.7, June 25, 2022, event, its full moment tensor (Section 4.3.1) was compared with the full moment tensors of six suspected blasts (Section 4.3.2) and the EQ event (Section 4.3.3). Figure 12 shows the average percentages of the ISO, CLVD, and DC components of the full moment tensors for all of these events.

The first thing to notice is the difference in the moment tensors between the ML = 3.7, June 25, 2022, event (large non-DC component, small DC component) and the EQ event in 2016 (small non-DC component, large DC component). Previous studies have shown that seismic events unrelated to mining blasts often have a large DC component, indicating significant shearing motion on a discontinuity or the fault plane of a pre-existing fault (Caputa and Rudzinski, 2019). The large DC component for the EQ event and the small DC component for the ML = 3.7, June 25, 2022, event implies that the main source mechanism of the ML = 3.7, June 25, 2022, event was not shearing motion. In other words, this event should not be considered a tectonic earthquake unrelated to blasting.

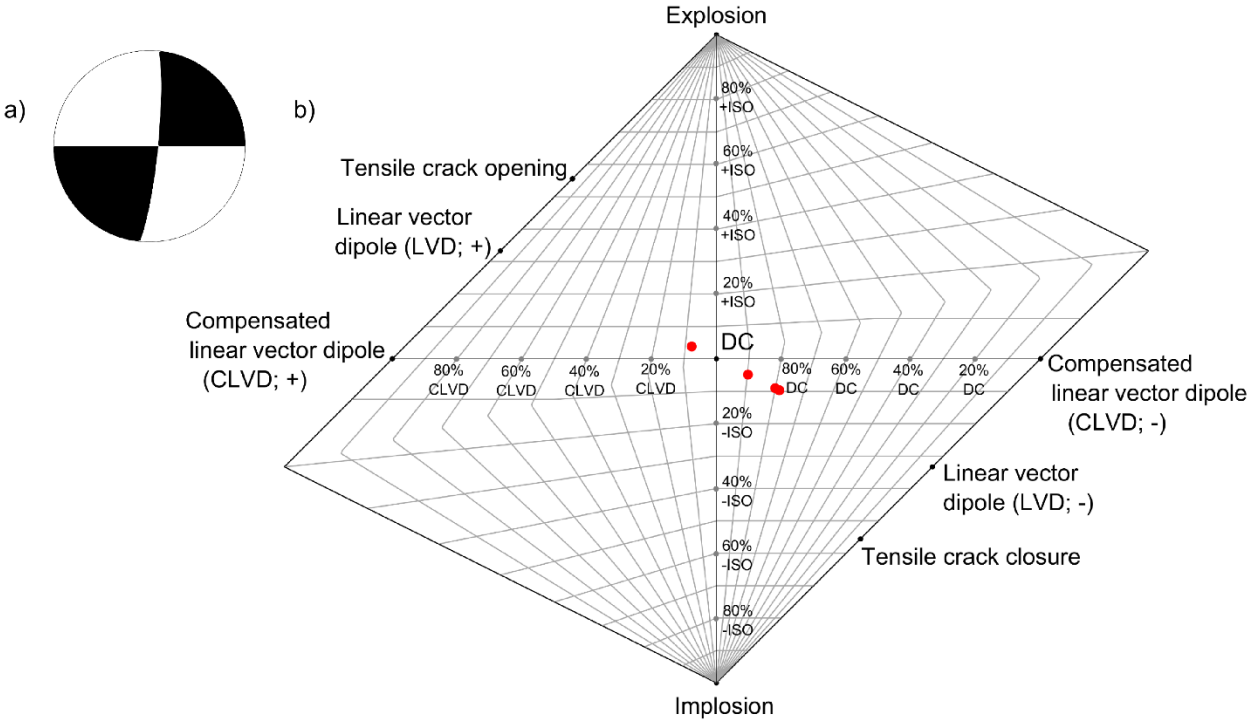

Figure 10. Moment tensor inversion results for the earthquake event (local magnitude 1.68) near Hinton on May 4, 2016: (a) beachball plot; (b) Hudson's source–type plot with solutions shown as red dots. Abbreviations: DC, double couple; ISO, isotropic.

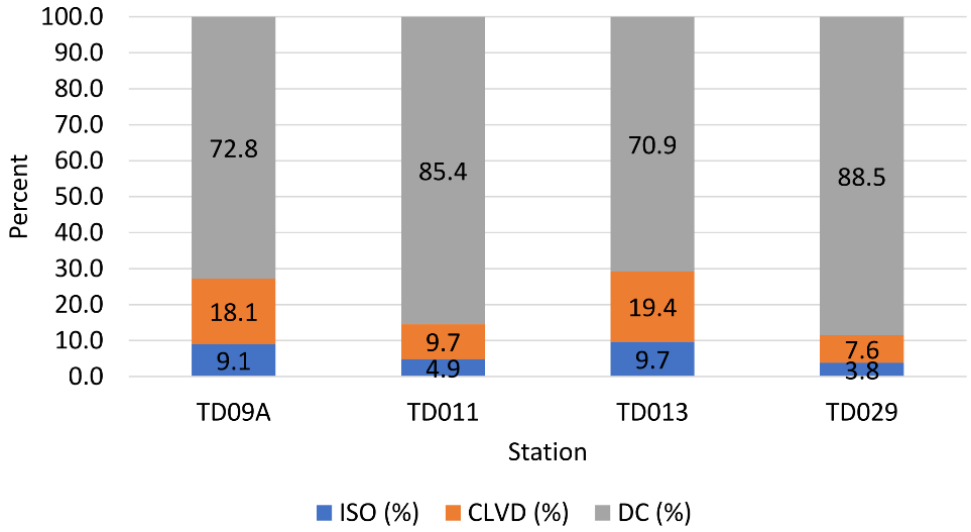

Figure 11. Moment tensor decomposition results for the earthquake event (local magnitude 1.68) near Hinton on May 4, 2016. See Figure 3 for locations of event and stations. Abbreviations: CLVD, compensated linear vector dipole; DC, double-couple; ISO, isotropic.

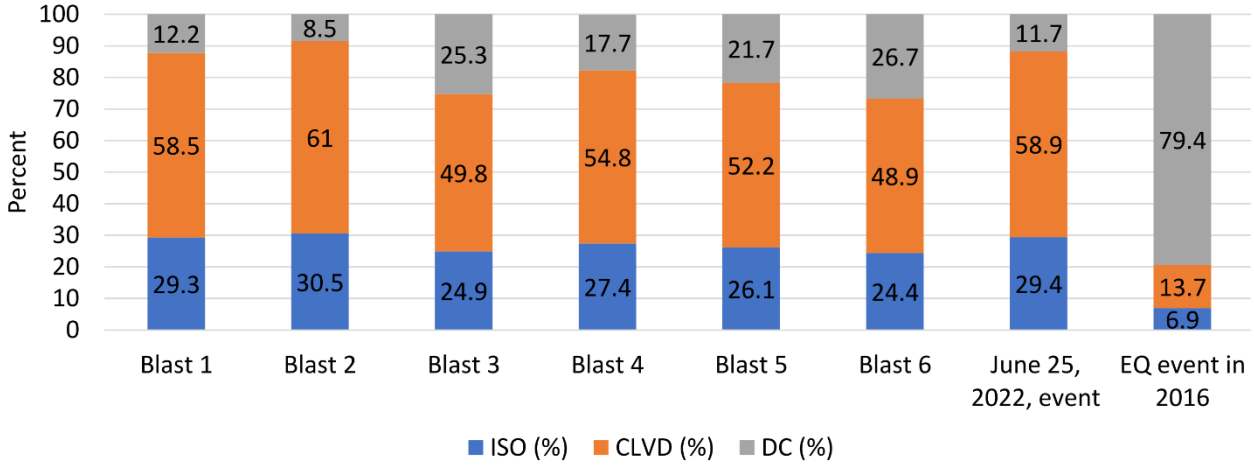

Figure 12. Comparison of the moment tensors for six suspected blasts, the June 25, 2022, event, and the earthquake (EQ) event on May 4, 2016. Abbreviations: CLVD, compensated linear vector dipole; DC, double-couple; ISO, isotropic.

Also noticeable are interesting similarities between the ML = 3.7, June 25, 2022, event and the six suspected blasts; all events have statistically significant non-DC components and small DC components. Previous studies also demonstrated that seismic events related to blasting are often characterized by significant non-DC components (Dreger et al., 2008; Caputa et al., 2015; Rudziński et al., 2016; Caputa and Rudzinski, 2019). Additionally, Kühn and Vavryčuk (2013) showed that a small DC component (shear faulting triggered during blasting) could not be excluded from the full moment tensor. Thus, the large non-DC and small DC components suggest that the source mechanism of the ML = 3.7, June 25, 2022, event was primarily related to a detonation(s).

5 Discussions

5.1 Timing of the Event

By inspecting the timing of the event and nearby blasting, it is possible to determine if the M_L = 3.7, June 25, 2022, event could have been associated with a blast. Based on the information provided by the mining company operating in the area, the blast occurred at 23:30:59 UTC, June 25, 2022. The approximate distance between the blast and the closest station, RV.YELLA, is 30 km. The arrival of P-waves at this station were recorded at 23:31:04 UTC. Assuming an average Vp of 4.5 km/s, it would have taken approximately 6 s for these P-waves to arrive at RV.YELLA station, indicating that the origin time (origin time is defined as the time of the initial energy release of a seismic event [Lomax et al., 2009]) of these P-waves was approximately 23:30:59 UTC. This means the M_L = 3.7, June 25, 2022, event, which occurred at 23:30:59 UTC, happened at approximately 0 s of the blast. Since detonation could not cause an induced seismic event at t = 0 s (Caputa et al., 2015; Caputa and Rudzinski, 2019), the M_L = 3.7, June 25, 2022, event cannot be a separate event induced by blasting. The timing of the event strongly supports the classification from moment tensor analysis that this event was a blast.

5.2 Interpretation of the Large CLVD Component

It is often expected that blasts exhibit a large positive ISO component and a small DC component (Kühn and Vavryčuk, 2013). Previous studies also demonstrate that a larger positive CLVD component could be observed in the moment tensor of blast events (Caputa et al., 2015; Caputa and Rudzinski, 2019). In this study, the M_L = 3.7, June 25, 2022, event and the six suspected blasts all have the large positive CLVD (linear dilatation) components (60%), followed by smaller ISO (30%) and DC (20%) components in the moment tensors. Caputa et al. (2015) and Caputa and Rudzinski (2019) suggested that the linear extension might be related to stress redistribution near the excavation area. The ISO component is relatively large and positive for the blasts, indicating the large volume changes (compression due to blasting) in the source (Caputa et al., 2015; Caputa and Rudzinski, 2019).

5.3 Estimating the June 25, 2022, Event's Moment Magnitude from M_0 and M_L

Table 3 shows the M_W, calculated from the M_0 (Equation 11), for the 18 stations that recorded the data studied for the M_L = 3.7, June 25, 2022, event. The average M_W is 3.6.

Table 3. Moment magnitude (M_W), derived from moment tensor analysis, for the 18 stations that recorded the data studied for the M_L = 3.7, June 25, 2022, event, central Alberta. See Table 4 in Appendix 1 for station locations.

No.	Station	M_W	No.	Station	M_W
1	DEDWA	3.8	10	PECRA	3.7
2	EGLEA	3.5	11	TD008	3.7
3	FAIRA	3.6	12	BRLDA	3.6
4	HSPGA	3.5	13	SNUFA	3.5
5	KW003	3.9	14	TONYA	3.4
6	KW006	3.6	15	BDMTA	3.2
7	KW008	3.7	16	STPRA	3.9
8	KW010	3.9	17	TD002	3.5
9	LDM	2.9	18	WTMTA	3.5

The M_W obtained from the moment tensor analysis is considered the most robust estimate of the event's strength (Ristau et al., 2005). This result was compared with the moment magnitude estimated from the M_L and the scaling relation (Equation 13).

The AGS estimated an M_L of 3.7 for the June 25, 2022, event using the seismic data from the regional seismic network (see Stern et al., 2013, for AGS estimation process) and the magnitude formula proposed by Yenier (2017). Based on this M_L, the M_W for this event was estimated using Equation 13:

$$M_w = 0.754 \times M_L + 0.88 = 0.754 \times 3.7 + 0.88 \approx 3.67. \quad (16)$$

This result is comparable with the $M_W = 3.6$ obtained from the moment tensor analysis.

6 Conclusions

The moment tensor analysis of the local magnitude (M_L) = 3.7, June 25, 2022, event shows consistent results between multiple stations, with a large non–double-couple (DC) component (29.4% isotropic [ISO] and 58.9% compensated linear vector dipole [CLVD]) and a small DC component (11.7%). The three basic components of its full moment tensor show that the largest value of the CLVD component (linear dilatation) might be associated with stress redistribution near an excavation area. The relatively large ISO component indicates large volume changes in the source. The small DC component implies minor shear faulting triggered by the blast. This event signature is similar to the moment tensors of events previously identified as suspected blasts and contrasts with the moment tensor of a tectonic earthquake in the area. The comparison reveals that the source mechanism of the $M_L = 3.7$, June 25, 2022, event was predominantly related to a detonation. The blasting time is exactly the same as the event time, suggesting that the blast did not induce an earthquake as there would be a lag between the blast and the earthquake. Rather, the seismic event detected was the actual blast. The moment tensor analysis also provided an average moment magnitude of 3.6 for the event. This moment magnitude aligns with the moment magnitude calculated from the local magnitude estimated by the AGS for the June 25, 2022, event. Based on all of this evidence, the $M_L = 3.7$, June 25, 2022, event is classified as the largest mining blast recorded in Alberta, to date. The results of this analysis show that moment tensor analysis can help discriminate between blast-related events and tectonic events in Alberta.

7 References

Aki, K. and Richards, P.G. (2002): Quantitative seismology (2nd edition); University Science Books, Meville, New York, 700 p.

Anton, H. (1999): Calculus: a new horizon (6th edition); Wiley, New York, New York, 912 p.

Baig, A. and Urbancic, T. (2010): Microseismic moment tensors: a path to understanding frac growth; The Leading Edge, v. 29, no. 3, p. 320–324, doi:10.1190/1.3353729.

Bormann, P., Engdahl, E.R. and Kind, R. (2012): Seismic wave propagation and earth models; Chapter 2 *in* New manual of seismological observatory practice (NMSOP-2), P. Bormann (ed.), GFZ German Research Centre for Geosciences, Potsdam, Germany, 105 p.

Caputa, A. and Rudziński, L. (2019): Source analysis of post-blasting events recorded in deep copper mine, Poland; Pure and Applied Geophysics, v. 176, no. 8, p. 3451–3466, doi:10.1007/s00024-019-02171-x.

Caputa, A., Talaga, A. and Rudzinski, L. (2015): Analysis of post-blasting source mechanisms of mining induced seismic events in Rudna copper mine, Poland; Contemporary Trends in Geoscience, v. 4, p. 26–38, doi:10.1515/ctg-2015-0003.

Červený, V. (2001): Seismic ray theory; Cambridge University Press, Cambridge, United Kingdom, 713 p.

D'Alessandro, A. and Stickney, M. (2012): Montana seismic network performance: an evaluation through the SNES method; Bulletin of the Seismological Society of America, v. 102, no. 1, p. 73–87, doi:10.1785/0120100234.

Dreger, D.S., Ford, S.R. and Walter, W.R. (2008): Source analysis of the Crandall Canyon, Utah, mine collapse; Science, v. 321, no. 5886, p. 217, doi:10.1126/science.1157392.

Eaton, D.W., van der Baan, M., Birkelo, B. and Tary, J.-B. (2014): Scaling relations and spectral characteristics of tensile microseisms: evidence for opening/closing cracks during hydraulic fracturing; Geophysical Journal International, v. 196, no. 3, p. 1844–1857, doi:10.1093/gji/ggt498.

Eyre, T.S. and van der Baan, M. (2015): Overview of moment tensor inversion of microseismic events; The Leading Edge, v. 34, no. 8, p. 882–888, doi:10.1190/tle34080882.1.

Eyre, T.S. and van der Baan, M. (2017): The reliability of microseismic moment-tensor solutions: surface versus borehole monitoring; Geophysics, v. 82, no. 6, p. KS113–KS125, doi:10.1190/geo2017-0056.1.

Forouhideh, F. and Eaton, D.W. (2009): Microseismic monitoring: insights from moment tensor inversion; CREWES Research Report, v. 21, 19 p., URL <https://www.crewes.org/Documents/ResearchReports/2009/CRR200921.pdf> [September 2022].

Hardebeck, J.L. and Shearer, P.M. (2003): Using S/P amplitude ratios to constrain the focal mechanisms of small earthquakes; Bulletin of the Seismological Society of America, v. 93, no. 6, p. 2434–2444, doi:10.1785/0120020236.

Hudson, J., Pearce, R. and Rogers, R. (1989): Source type plot for inversion of the moment tensor; Journal of Geophysical Research: Solid Earth, v. 94, no. B1, p. 765–774, doi:10.1029/jb094ib01p00765.

Jost, M.L. and Herrmann, R.B. (1989): A student's guide to and review of moment tensors; Seismological Research Letters, v. 60, no. 2, p. 37–57, doi:10.1785/gssrl.60.2.37.

Julian, B.R. and Foulger, G. (1996): Earthquake mechanisms from linear-programming inversion of seismic-wave amplitude ratios; Bulletin of the Seismological Society of America, v. 86, no. 4, p. 972–980, doi:10.1785/bssa0860040972.

Kisslinger, C. (1980): Evaluation of S to P amplitude rations for determining focal mechanisms from regional network observations; Bulletin of the Seismological Society of America, v. 70, no. 4, p. 999–1014, doi:10.1785/bssa0700040999.

Knopoff, L. and Randall, M.J. (1970): The compensated linear vector dipole: a possible mechanism for deep earthquakes; Journal of Geophysical Research, v. 75, no. 26, p. 4957–4963, doi:10.1029/jb075i026p04957.

Kühn, D. and Vavryčuk, V. (2013): Determination of full moment tensors of microseismic events in a very heterogeneous mining environment; Tectonophysics, v. 589, p. 33–43, doi:10.1016/j.tecto.2012.12.035.

Lomax, A., Michelini, A. and Curtis, A. (2009): Earthquake location, direct, global-search methods; Encyclopedia of Complexity and Systems Science, v. 5, p. 2449–2473, doi:10.1007/978-0-387-30440-3_150.

Maxwell, S. (2014): Microseismic imaging of hydraulic fracturing: improved engineering of unconventional shale reservoirs; Society of Exploration Geophysicists, Tulsa, Oklahoma, Distinguished Instructor Series, no. 17, 197 p.

Menke, W. (1989): Geophysical data analysis: discrete inverse theory (revised edition); Academic Press Inc., New York, New York, 285 p.

Ristau, J., Rogers, G.C. and Cassidy, J.F. (2005): Moment magnitude-local magnitude calibration for earthquakes in western Canada; Bulletin of the Seismological Society of America, v. 95, no. 5, p. 1994–2000, doi:10.1785/0120050028.

Ross, Z.E., Ben-Zion, Y., White, M.C. and Vernon, F.L. (2016): Analysis of earthquake body wave spectra for potency and magnitude values: implications for magnitude scaling relations; Geophysical Journal International, v. 207, no. 2, p. 1158–1164, doi:10.1093/gji/ggw327.

Rudziński, L., Cesca, S. and Lizurek, G. (2016): Complex rupture process of the 19 March 2013, Rudna mine (Poland) induced seismic event and collapse in the light of local and regional moment tensor inversion; Seismological Research Letters, v. 87, no. 2A, p. 274–284, doi:10.1785/0220150150.

Schultz, R.J. and Stern, V.H. (2015): The Regional Alberta Observatory for Earthquake Studies Network (RAVEN); CSEG Recorder, v. 40, no. 8, p. 34–37, URL <http://csegrecorder.com/articles/view/the-regional-alberta-observatory-for-earthquake-studies-network-raven> [September 2022].

Schultz, R.J., Yusifbayov, J. and Shipman, T.C. (2020): The scientific induced seismicity monitoring network (SCISMN); Alberta Energy Regulator / Alberta Geological Survey, AER/AGS Open File 2019-09, 10 p., URL <https://ags.aer.ca/publication/ofr-2019-09> [September 2022].

Seismological Facility for the Advancement of Geoscience (2018): Frequently answered question: what is a “count” in timeseries data?: EarthScope Consortium, Inc., URL <https://ds.iris.edu/ds/support/faq/6/what-is-a-count-in-timeseries-data/> [January 2024].

Stein, S. and Wysession, M. (2003): An introduction to seismology, earthquakes, and earth structure; Blackwell Publishing, Malden, Massachusetts, 498 p.

Stern, V.H., Schultz, R.J., Shen, L., Gu, Y.J. and Eaton, D.W. (2013): Alberta Earthquake Catalogue, Version 1.0: September 2006 through December 2010; Alberta Energy Regulator, AER/AGS Open File Report 2013-15, 29 p., URL <https://ags.aer.ca/publication/ofr-2013-15> [September 2022].

Van Dok, R., Fuller, B., Engelbrecht, L. and Sterling, M. (2011): Seismic anisotropy in microseismic event location analysis; The Leading Edge, v. 30, no. 7, p. 766–770, doi:10.1190/1.3609091.

Vavryčuk, V. (2011): Tensile earthquakes: theory, modeling, and inversion; Journal of Geophysical Research: Solid Earth, v. 116, no. B12, art. B12320, doi:10.1029/2011jb008770.

Vavryčuk, V. (2015): Moment tensors: decomposition and visualization; *in* Encyclopedia of earthquake engineering, M. Beer, I.A. Kougiomtzoglou, E. Patelli and S.K. Au (ed.), Springer-Verlag, Berlin, Heidelberg, Germany, p. 1546–1559, doi:10.1007/978-3-642-35344-4_288.

Yenier, E. (2017): A local magnitude relation for earthquakes in the Western Canada Sedimentary Basin; Bulletin of the Seismological Society of America, v. 107, no. 3, p. 1421–1431, doi:10.1785/0120160275.

Appendix 1 – Station/Event Locations and Moment Tensor Decomposition Results

Table 4. Station locations in central Alberta and corresponding instrument scale factors. Abbreviations: 2K, Scientific Induced Seismicity Monitoring Network; MB, Montana Regional Seismic Network; RV, Regional Alberta Observatory for Earthquake Studies Network; TD, TransAlta Monitoring Network.

No.	Station	Latitude (°)	Longitude (°)	UTM Easting (m)	UTM Northing (m)	Scale Factor
1	2K.KW002	54.6019	-118.5939	397037.91	6051660.24	2.90E+08
2	2K.KW003	54.4622	-118.3042	415462.45	6035731.23	2.90E+08
3	2K.KW006	54.4906	-118.7503	386627.61	6039518.10	2.90E+08
4	2K.KW008	54.6333	-118.6542	393225.28	6055243.72	2.90E+08
5	2K.KW010	54.5554	-118.4402	406859.84	6046272.34	2.90E+08
6	MB.LDM	48.4538	-115.3191	624281.87	5368104.80	1.70E+08
7	RV.BDMTA	54.8129	-118.9149	376945.00	6075652.29	3.02E+08
8	RV.BRLDA	54.0920	-117.4033	473622.26	5993832.90	3.02E+08
9	RV.DEDWA	56.6446	-117.3891	476138.21	6277893.26	3.00E+08
10	RV.EGLEA	54.4571	-116.4405	536271.83	6034524.87	3.00E+08
11	RV.FAIRA	56.1087	-118.8648	384030.88	6219744.51	2.99E+08
12	RV.HSPGA	49.3593	-113.6523	743072.22	5472789.98	3.02E+08
13	RV.KAKWA	54.4210	-118.9817	371422.95	6032172.73	2.99E+08
14	RV.PECRA	56.2956	-117.0270	498328.94	6238980.19	2.99E+08
15	RV.SNUFA	54.6781	-117.5398	465194.06	6059105.44	2.99E+08
16	RV.STPRA	55.6606	-115.8323	573460.61	6168927.69	3.02E+08
17	RV.SWHSA	54.8994	-116.7518	515916.67	6083625.05	3.02E+08
18	RV.TONYA	54.4054	-117.4908	468139.82	6028734.71	2.99E+08
19	RV.WTMTA	55.6942	-119.2398	359220.63	6174319.19	2.99E+08
20	RV.YELLA	53.2367	-117.1408	490602.62	5898611.23	3.02E+08
21	TD.TD002	53.4394	-114.3876	673516.63	5924330.27	3.01E+08
22	TD.TD008	52.8041	-115.4318	605714.68	5851631.17	3.01E+08
23	TD.TD009	52.3206	-116.3234	546118.07	5796910.53	3.01E+08
24	TD.TD09A	52.9250	-116.3897	541028.19	5864101.79	3.01E+08
25	TD.TD011	52.5494	-115.5157	600642.95	5823181.93	3.01E+08
26	TD.TD013	52.5179	-115.0234	634116.29	5820479.16	3.01E+08
27	TD.TD029	52.2171	-115.2001	622960.46	5786711.78	3.01E+08

Table 5. Locations of the local magnitude 3.7, June 25, 2022, event, six suspected blasts, and the earthquake (EQ) event near Hinton in 2016, central Alberta.

Event	Latitude (°)	Longitude (°)	UTM Easting (m)	UTM Northing (m)	Depth (m)
June 25, 2022	53.4037	-117.3185	479390.38	5917225.12	0
Blast 1	53.3744	-117.3237	478464.79	5913969.58	0
Blast 2	53.3692	-117.3378	477524.01	5913395.44	0
Blast 3	53.3836	-117.3440	477119.20	5914999.38	0
Blast 4	53.4106	-117.3478	476881.09	5918004.32	0
Blast 5	53.4209	-117.3576	476235.41	5919153.40	0
Blast 6	53.4284	-117.2953	480379.05	5919968.83	0
EQ in 2016	53.3760	-117.2100	486029.57	5914119.30	5000

Table 6. Moment tensor decomposition results for the local magnitude 3.7, June 25, 2022, event, central Alberta. Abbreviations: 2K, Scientific Induced Seismicity Monitoring Network; CLVD, compensated linear vector dipole; DC, double-couple; MB, Montana Regional Seismic Network; ISO, isotropic; RV, Regional Alberta Observatory for Earthquake Studies Network; TD, TransAlta Monitoring Network.

		Component		
No.	Station	ISO (%)	CLVD (%)	DC (%)
1	2K.KW003	-22.0	-44.0	34.0
2	2K.KW006	18.7	37.4	44.0
3	2K.KW008	32.9	65.8	1.3
4	2K.KW010	26.2	52.4	21.4
5	MB.LDM	29.8	59.7	10.5
6	RV.BDMTA	30.6	61.2	8.1
7	RV.BRLDA	32.1	64.2	3.8
8	RV.DEDWA	-33.2	-66.5	0.3
9	RV.EGLEA	33.1	66.2	0.6
10	RV.FAIRA	32.8	65.7	1.5
11	RV.HSPGA	22.5	44.9	32.6
12	RV.PECRA	33.1	66.2	0.8
13	RV.SNUFA	-31.9	-63.7	4.4
14	RV.STPRA	27.3	54.6	18.1
15	RV.TONYA	33.2	66.4	0.4
16	RV.WTMTA	30.7	61.5	7.8
17	TD.TD002	-32.7	-65.4	2.0
18	TD.TD008	-27.0	-53.9	19.1
Average (of absolute values)		29.4	58.9	11.7

Table 7. Moment tensor decomposition results for blast 1, April 24, 2022, central Alberta. Abbreviations: 2K, Scientific Induced Seismicity Monitoring Network; CLVD, compensated linear vector dipole; DC, double-couple; ISO, isotropic; RV, Regional Alberta Observatory for Earthquake Studies Network; TD, TransAlta Monitoring Network.

		Component		
No.	Station	ISO (%)	CLVD (%)	DC (%)
1	2K.KW002	-23.8	-47.5	28.7
2	2K.KW008	28.9	57.7	13.4
3	RV.BDMTA	32.7	65.4	1.8
4	RV.BRLDA	27.3	54.7	18.0
5	RV.KAKWA	-32.3	-64.6	3.1
6	RV.SNUFA	-33.3	-66.6	0.1
7	RV.TONYA	-27.3	-54.6	18.2
8	TD.TD002	-30.8	-61.7	7.5
9	TD.TD008	-27.0	-53.9	19.1
Average (of absolute values)		29.3	58.5	12.2

Table 8. Moment tensor decomposition results for blast 2, April 30, 2022, central Alberta. Abbreviations: 2K, Scientific Induced Seismicity Monitoring Network; CLVD, compensated linear vector dipole; DC, double-couple; ISO, isotropic; RV, Regional Alberta Observatory for Earthquake Studies Network; TD, TransAlta Monitoring Network.

		Component		
No.	Station	ISO (%)	CLVD (%)	DC (%)
1	2K.KW002	27.4	54.9	17.7
2	2K.KW003	-32.0	-64.0	4.1
3	RV.BRLDA	32.4	64.9	2.7
4	RV.EGLEA	31.8	63.5	4.7
5	RV.FAIRA	29.9	59.8	10.3
6	RV.KAKWA	-28.2	-56.5	15.3
7	RV.SNUFA	27.5	54.9	17.6
8	RV.WTMTA	-32.0	-64.0	4.0
9	TD.TD002	33.2	66.5	0.3
Average (of absolute values)		30.5	61.0	8.5

Table 9. Moment tensor decomposition results for blast 3, May 23, 2022, central Alberta. Abbreviations: 2K, Scientific Induced Seismicity Monitoring Network; CLVD, compensated linear vector dipole; DC, double-couple; ISO, isotropic; RV, Regional Alberta Observatory for Earthquake Studies Network.

		Component		
No.	Station	ISO (%)	CLVD (%)	DC (%)
1	2K.KW002	-22.1	-44.2	33.7
2	RV.EGLEA	-30.5	-61.0	8.5
3	RV.KAKWA	-18.4	-36.7	44.9
4	RV.SNUFA	31.5	63.0	5.5
5	RV.SWHSA	-26.8	-53.7	19.5
6	RV.YELLA	-20.1	-40.3	39.6
Average (of absolute values)		24.9	49.8	25.3

Table 10. Moment tensor decomposition results for blast 4, July 8, 2022, central Alberta. Abbreviations: 2K, Scientific Induced Seismicity Monitoring Network; CLVD, compensated linear vector dipole; DC, double-couple; ISO, isotropic; RV, Regional Alberta Observatory for Earthquake Studies Network; TD, TransAlta Monitoring Network.

		Component		
No.	Station	ISO (%)	CLVD (%)	DC (%)
1	2K.KW002	-16.9	-33.7	49.4
2	2K.KW003	30.3	60.7	9.0
3	RV.BDMTA	19.0	38.0	43.1
4	RV.BRLDA	33.0	66.0	1.0
5	RV.EGLEA	31.4	62.9	5.7
6	RV.SWHSA	-33.3	-66.6	0.0
7	RV.YELLA	-24.6	-49.2	26.2
8	TD.TD002	33.0	66.0	1.1
9	TD.TD008	-20.7	-41.4	38.0
10	TD.TD009	-32.0	-64.0	4.0
Average (of absolute values)		27.4	54.8	17.7

Table 11. Moment tensor decomposition results for blast 5, July 16, 2022, central Alberta. Abbreviations: 2K, Scientific Induced Seismicity Monitoring Network; CLVD, compensated linear vector dipole; DC, double-couple; ISO, isotropic; RV, Regional Alberta Observatory for Earthquake Studies Network.

		Component		
No.	Station	ISO (%)	CLVD (%)	DC (%)
1	2K.KW002	-17.4	-34.7	47.9
2	2K.KW003	-28.2	-56.5	15.3
3	RV.BRLDA	-33.2	-66.4	0.4
4	RV.EGLEA	31.6	63.2	5.1
5	RV.YELLA	-20.1	-40.3	39.6
Average (of absolute values)		26.1	52.2	21.7

Table 12. Moment tensor decomposition results for blast 6, July 19, 2022, central Alberta. Abbreviations: 2K, Scientific Induced Seismicity Monitoring Network; CLVD, compensated linear vector dipole; DC, double-couple; ISO, isotropic; RV, Regional Alberta Observatory for Earthquake Studies Network; TD, TransAlta Monitoring Network.

		Component		
No.	Station	ISO (%)	CLVD (%)	DC (%)
1	2K.KW002	-20.9	-41.7	37.4
2	2K.KW003	18.9	37.8	43.2
3	2K.KW008	19.4	38.8	41.8
4	RV.KAKWA	-17.4	-34.8	47.7
5	RV.SWHSA	-29.9	-59.8	10.3
6	RV.YELLA	-29.2	-58.5	12.3
7	TD.TD002	-31.9	-63.8	4.2
8	TD.TD008	-27.9	-55.8	16.2
Average (of absolute values)		24.4	48.9	26.7

Table 13. Moment tensor decomposition results for the earthquake event near Hinton, May 4, 2016, central Alberta. Abbreviations: CLVD, compensated linear vector dipole; DC, double-couple; ISO, isotropic; TD, TransAlta Monitoring Network.

No.	Station	Component		
		ISO (%)	CLVD (%)	DC (%)
1	TD.TD09A	9.1	18.1	72.8
2	TD.TD011	4.9	9.7	85.4
3	TD.TD013	9.7	19.4	70.9
4	TD.TD029	3.8	7.6	88.5
Average (of absolute values)		6.9	13.7	79.4